Check for updates

Received: 25 August 2019 | Revised: 28 December 2019 | Accepted: 28 December 2019
DOI: 10.1002/er.5164

RESEARCH ARTICLE

INTERNATIONAL JOURNAL OF ENERGY RESEARCH WILEY

Bluff body with built-in piezoelectric cantilever for flow-induced energy harvesting

Min Zhang[1#] | **Guobiao Hu**[2#] | **Junlei Wang**[3,4]

[1]School of Shipping and Naval Architecture, Chongqing Jiaotong University, Chongqing, China
[2]Department of Mechanical Engineering, The University of Auckland, Auckland, New Zealand
[3]School of Mechanical and Power Engineering, Zhengzhou University, Zhengzhou, China
[4]Soyotec Technologies Co., Ltd, Beijing, China

Correspondence
Jun-lei Wang, School of Mechanical and Power Engineering, Zhengzhou University, Zhengzhou 450000, China.
Email: jlwang@zzu.edu.cn

Funding information
National Natural Science Foundation of China, Grant/Award Numbers: 51977196, 51606171

Summary

This paper investigates a flow-induced vibration energy harvester comprising a piezoelectric beam (piezo-beam) installed within a hollow circular cylinder. Under the flow excitation, the energy-harvesting system including the cylinder and the piezo-beam vibrates and generates electricity. A lumped parametric model incorporating the fluid-structure interaction (FSI) is developed to evaluate the performance of the proposed energy harvester. Based on the theoretical analysis, several guidelines on the design and optimization of the proposed energy harvester are provided. Subsequently, a numerical model is used to simulate the FSI between the proposed system and the external flow field. Finally, a physical prototype is fabricated and an experiment is conducted to test the actual performance for validation. The theoretical analysis results are verified by the numerical and experimental results.

KEYWORDS

built-in cantilever cylinder, energy harvesting, flow-induced vibration, piezoelectric

1 | INTRODUCTION

In the past two decades, the piezoelectric energy scavenging technology has been an ever-increasing focus due to its potential for letting micro-electro-mechanical systems (MEMS)[1-7] to get rid of chemical batteries. This technology can be an alternative of the chemical batteries that require to be frequently recharged or replaced from the sensors and devices. Under such a context, various methods have been developed to model and analyse piezoelectric energy harvesters (PEHs).[8-10] On the other hand, various performance enhancement methods for vibration energy harvesting have been extensively explored, including using multimodal techniques, nonlinear mechanisms, and active tuning strategies.[11-17]

Fluid flow ubiquitously exists in the environment and could be converted to structural vibrations.[18,19] Based on the mechanism of flow-induced vibration, researchers have proposed various aeroelastic PEHs.[20,21] Amini et al[22] presented an accurate numerical method for modelling a PEH placed in fluid flow. An experiment was carried out to validate the numerical model. Erturk et al[23] proposed an energy harvester that is composed of a curved airfoil section bonded with a piezoelectric patch. The theoretical and experimental results matched well and validated the potential of the proposed system for energy harvesting. Akaydin et al[24,25] examined the performance of a vortex-induced vibration (VIV) PEH that comprised a hollow cylinder and a cantilever beam. Under the wind with a speed of 1.192 m/s, the proposed energy harvester generated a power output of 0.1 mW. Dai et al[26,27] presented a theoretical study of a VIV-PEH that comprises a piezo-beam and a round-shaped bluff body. The governing equation was derived using the Euler-Lagrange principle. Yang et al[28] investigated various bluff body cross-sections for harvesting energy from

---

[#]These authors contribute equally to this work.

© 2020 John Wiley & Sons, Ltd.

galloping. The square-sectioned one exhibited the advantages of decreasing the threshold wind speed and improving the high-peak power output. Zhang et al[29] presented a wake-induced vibration (WIV) PEH. The experiment showed that there existed an optimal configuration of the cylinders for maximizing the output voltage and power. Wang et al[30] proposed a novel wind energy harvester by loading the bluff body with Y-shaped attachments. The VIV was transformed into galloping and the energy-harvesting performance was proved to be enhanced. Molino-Minero-Re et al[31] mounted a series of cylinders on a cantilever beam and estimated the energy output from the VIVs of the cylinders. The preliminary results showed that some of the configurations can generate a power of up to 0.31 μW. Mehmood et al[32] harnessed energy from the VIV at low Reynolds numbers. The results showed that increasing the load resistance widens the synchronization region. Zhang et al[33] built the flow-machine-electric coupling model for the PEH. The model was established by combining the steady and quasi-steady VIV model and lumped electromechanical model. It was found that increasing the size of the cylinder increases the harvested power.

Research on VIV-based and WIV-based energy harvesting shows that there are two common features of these two cases. First, an optimal velocity exists in achieving the maximum vibration amplitude and power output efficiency.[34] Second, there is a certain lock-in range that can be classified into several different evolution stages.[35,36] The energy harvesters in the above literatures are composed of bluff bodies and piezo-beams, and the adverse effects of splitter plate[37] will inevitably occur due to the connection of the piezo-beam, resulting in the decline of the vibration intensity. Although the piezo-beam width is smaller than the cylinder length, there is a relative motion between the piezo-beam and the surrounding fluid field during transverse vibration. The structure-fluid interaction interferes the flow field, and thus affects the energy conversion efficiency.[4] Moreover, the fluid damping has a great influence due to the large dynamic viscosity of water when the energy harvester operates underwater. In addition, an insulation coating is needed to be designed for the protection of underwater devices. However, research on this topic is still rare.

This paper proposes a novel flow-induced vibration PEH with an insulation coating. The piezo-beam acting as the energy generator is placed within a hollow cylinder. The external flow directly interacts with the cylinder rather than the piezo-beam. The piezo-beam does not directly interfere the flow field but the cylinder does. The flow separation of the piezo-beam is thus avoided. In addition, the built-in design makes the cylinder system to protect the piezo-beam from external debris and corrosion.

2 | THEORETICAL MODELLING

Figure 1A shows the proposed energy harvester. One end of the piezo-beam is clamped within a hollow cylinder. The other end is attached with a mass block. Two springs horizontally connect the upper edge of the cylinder to the wall of the wind tunnel. The lower edge of the cylinder is tightened to the tunnel bottom wall through a spring to avoid cylinder inclination in the wind flow. Thus, the whole cylinder resembles a complex pendulum that can rotate around the *z*-axis. The incoming flow in the wind tunnel is parallel to the piezoelectric plate surface. Once the wind speed increases up to the threshold value, the cylinder begins to swing in the cross-stream direction under the fluid-structure interaction. The motion of the hollow cylinder plays the role as a base excitation for the built-in piezo-beam, driving it to vibrate and the electrical energy is generated through the direct piezoelectric effect.

2.1 | Electromechanical-coupled model

The cylinder can be equivalently viewed as a compound pendulum that swings around the *z*-axis during the entire working process. The *y*-component of elastic force by the front spring *k* provides the cylinder an additional restoring force, which is also considered in the oscillation equation of the cylinder. The internal piezo-beam is represented by a lumped electromechanical model that is composed of two degrees of freedom (DOFs), namely the displacement and the voltage. The entire system is thus

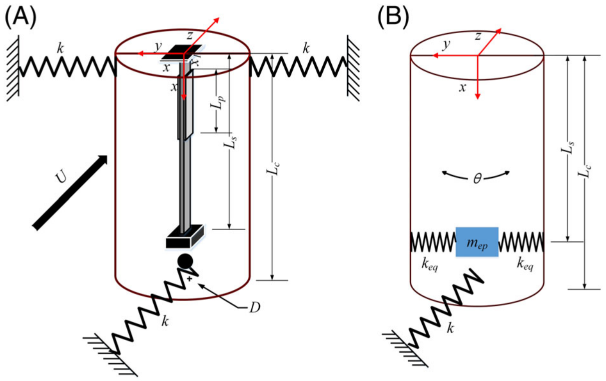

FIGURE 1 A, The schematic of the proposed vortex-induced vibration (VIV)-piezoelectric energy harvester (PEH); B, simplified model [Colour figure can be viewed at wileyonlinelibrary.com]

1099114x, 2020, 5, Downloaded from https://onlinelibrary.wiley.com/doi/10.1002/er.5164 by The Hong Kong University Of Science & Technology, Wiley Online Library on [17/04/2026]. See the Terms and Conditions (https://onlinelibrary.wiley.com/terms-and-conditions) on Wiley Online Library for rules of use; OA articles are governed by the applicable Creative Commons License

simplified as a lumped parameter model of three DOFs, which is shown in Figure 1B. The motion equation of the external cylinder is written as

$$J_z\frac{d^2\theta}{dt^2}+c\frac{d\theta}{dt}+\frac{1}{2}m_cL_cg\sin\theta+k_yL_c{}^2\sin\theta=M(t), \tag{1}$$

where $J_z = m_cD^2/8 + m_cL_c{}^2/3$ is the rotational inertia of the hollow cylinder about z axis, D is the diameter of the cross-section of the cylinder, $c = 2J_z\xi\omega_\mathrm{n}$ is the damping coefficient, m_c is the cylinder mass, k_y is the y-direction component of the stiffness of the front spring, $\omega_n = (m_cgL_c + 2k_yL_c{}^2)/2J_z$ is the natural frequency of the compound pendulum, and $M(t)$ is the moment of the transverse force. Considering small-amplitude oscillation of the cylinder, the governing equations of the entire system consisting of the motion equation of the compound pendulum (ie, the hollow cylinder) and the electromechanical equations of the piezo-beam can be written as

$$\begin{aligned}&J_z\frac{d^2\theta}{dt^2}+c\frac{d\theta}{dt}+\frac{1}{2}m_cL_cg\sin\theta+k_yL_c{}^2\sin\theta\\&+c_{eq}L_s{}^2\left(\frac{d\theta}{dt}-\frac{dy_s}{dt}\frac{1}{L_s}\right)+k_{eq}L_s{}^2(\theta-y_s/L_s)=M(t),\end{aligned} \tag{2}$$

$$m_{eq}\frac{d^2y_s}{dt^2}+c_{eq}\frac{dy_s}{dt}+k_{eq}y_s-\vartheta_{eq}V=\mu_1\left(c_{eq}\frac{d\theta}{dt}L_s+k_{eq}\theta L_s\right), \tag{3}$$

$$C_p\frac{dV}{dt}+\frac{V}{R}+\vartheta_{eq}\left(\frac{dy_s}{dt}-\frac{d\theta}{dt}L_s\right)=0, \tag{4}$$

where μ_1 is the correction coefficient of beam transverse vibration.[1] m_{eq}, c_{eq}, and k_{eq} represent the equivalent mass, damping coefficient, and stiffness, respectively. y_s is the tip displacement of the piezo-beam. C_p is the clamped capacitance, and ϑ_{eq} denotes the equivalent electromechanical coupling coefficient which can be calculated using the following equation:

$$\vartheta_{eq}=d_{31}k_{eq}b_pL_p(L_p+L_t)\frac{h_p+h_s}{I_p}, \tag{5}$$

where L_t is the length of the tip mass and I_p is the inertia moment of the cross-section of the piezo-beam.

2.2 | Aerodynamic effect

Considering a uniform flow of velocity U in the direction of z as shown in Figure 2, the fluid force $\delta F(t)$ exerted onto a section at x of the cylinder is the combination of drag δF_d and lateral lift δF_l.

Due to the movement of the cylinder, the direction of the flow and the direction of the exerted force deviate from each other and the angle of attack thus changes. As the lateral velocity varies along the cylinder length, the attack angle also changes accordingly. The deviation angle of δF_d and δF_l from the original directions is assumed to be α, then the lateral force on an elemental length δx of the cylinder at a distance x is

$$\delta F(t)=\delta F_d\sin\alpha+\delta F_l\cos\alpha. \tag{6}$$

The attack angle α is represented by the velocity vector diagram in Figure 3B and obtained below. Assuming α is small,

$$\sin\alpha=\frac{-\dot{y}}{\sqrt{U^2+\dot{y}^2}}\approx\frac{-\dot{y}}{U}, \tag{7}$$

$$\cos\alpha=\frac{U}{\sqrt{U^2+\dot{y}^2}}\approx 1. \tag{8}$$

According to Lighthill,[38] the lift δF_l in Equation (6) consists of the added inertia force δF_p and vortex-induced force δF_v, thus

$$\delta F(t)=\delta F_d\sin\alpha+\left(\delta F_p+\delta F_v\right)\cos\alpha. \tag{9}$$

In the current 2D model, the added inertia force equals

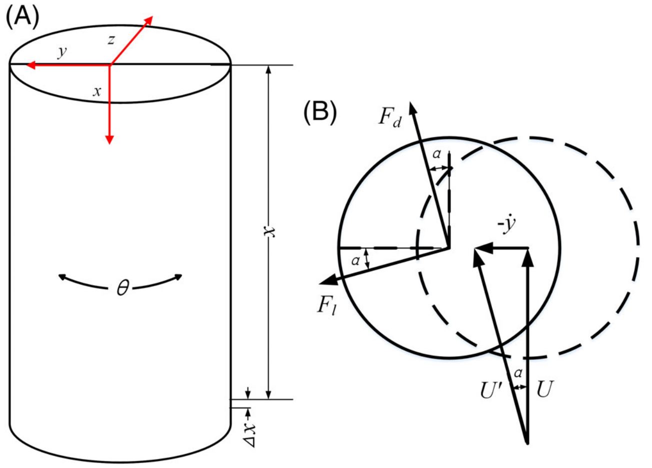

FIGURE 2 A, The cylinder bluff body; B, cross-sectional view of the force and velocity vector diagrams [Colour figure can be viewed at wileyonlinelibrary.com]

1099114x, 2020, 5, Downloaded from https://onlinelibrary.wiley.com/doi/10.1002/er.5164 by The Hong Kong University Of Science & Technology, Wiley Online Library on [17/04/2026]. See the Terms and Conditions (https://onlinelibrary.wiley.com/terms-and-conditions) on Wiley Online Library for rules of use; OA articles are governed by the applicable Creative Commons License

$$\delta F_p \cos\alpha = -C_A \frac{\rho_f \pi D^2 \delta x}{4} \ddot{y}, \tag{10}$$

where $C_A = 1$ is the added mass coefficient for an oscillating cylinder. The moment of the inertia force about the rotation axis can be calculated as

$$M_a = -J_a \frac{d^2\theta}{dt^2}. \tag{11}$$

The moment of inertia of the added mass is $J_a = \frac{m_a D^2}{16} + \frac{m_a L_c{}^2}{3}$, and the additional mass is $m_a = \frac{1}{4}\pi D^2 \rho_f L_c$. By defining C_L and C_D, respectively, as the lift and drag coefficients, we can rewrite δF_v and δF_d as

$$\delta F_v = C_L \frac{\rho_f D \delta x}{2} U^2, \tag{12}$$

$$\delta F_d = C_D \frac{\rho_f D \delta x}{2} U^2. \tag{13}$$

Substituting Equations (7), (8), (12), and (13) into Equation (9) and neglecting the potential force, we can obtain

$$\delta F(t) = C_L \frac{\rho_f D \delta x}{2} U^2 - C_D \frac{\rho_f D \delta x}{2} U \dot{y}. \tag{14}$$

Here, $\ddot{y}$ and $\dot{y}$ are, respectively, the transverse acceleration and velocity of the cylinder section at the distance of x measured from the rotation centre. Since the cylinder performs a swing motion, the relationship between transverse and angular accelerations are written as

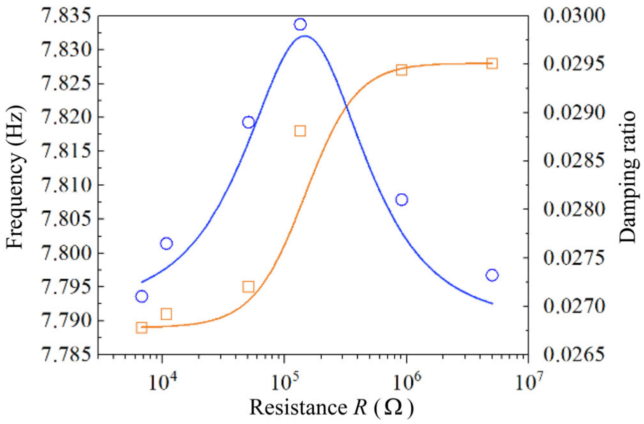

FIGURE 3 Damping ratios and natural frequency against load resistances. ◦, ξ of experiment; —, ξ of simulation; □, f_n of experiment; —, f_n of simulation [Colour figure can be viewed at wileyonlinelibrary.com]

$$\dot{y} = \frac{d\theta}{dt} x, \tag{15}$$

$$\ddot{y} = \frac{d^2\theta}{dt^2} x. \tag{16}$$

Inserting Equations (15) and (16) into Equation (14), one obtains

$$\delta F(t) = C_L \frac{\rho_f D \delta x}{2} U^2 - C_D \frac{\rho_f D \delta x}{2} U \frac{d\theta}{dt} x. \tag{17}$$

Subsequently, the moment of the transverse force without added inertia force on an infinitesimal section at the distance of x is

$$\delta M(t) = \left(C_L \frac{\rho_f D}{2} U^2 - C_D \frac{\rho_f D}{2} U \frac{d\theta}{dt} x \right) x \delta x. \tag{18}$$

By integrating $\delta M(t)'$ over the entire length of the cylinder, we can obtain the total moment on the cylinder as

$$M(t) = \int_0^{L_c} \delta M(t) = \int_0^{L_c} \left(C_L \frac{\rho_f D}{2} U^2 - C_D \frac{\rho_f D}{2} U \frac{d\theta}{dt} x \right) x \delta x, \tag{19}$$

$$M(t) = \frac{1}{4} \rho_f U^2 D C_L L_c{}^2 - \frac{1}{6} \rho_f U D C_D L_c{}^3 \frac{d\theta}{dt}. \tag{20}$$

Further, considering the influence of the additional mass, the total torque acting on the cylinder can be obtained by adding Equations (11) and (20) as follows:

$$M(t) = -J_a \frac{d^2\theta}{dt^2} + \frac{1}{4} \rho_f U^2 D C_L L_c{}^2 - \frac{1}{6} \rho_f U D C_D L_c{}^3 \frac{d\theta}{dt}. \tag{21}$$

By substituting Equation (21) into Equation (2), the PEH model under the flow-induced vibration is developed.

3 | EXPERIMENTAL STUDY AND PARAMETER IDENTIFICATION

A free decay test of the piezo-beam oscillation is first performed to determine the natural frequency and electromechanical coupling coefficient. The natural frequencies under open-circuit and short-circuit conditions can be used to calculate the

1099114x, 2020, 5, Downloaded from https://onlinelibrary.wiley.com/doi/10.1002/er.5164 by The Hong Kong University Of Science & Technology, Wiley Online Library on [17/04/2026]. See the Terms and Conditions (https://onlinelibrary.wiley.com/terms-and-conditions) on Wiley Online Library for rules of use; OA articles are governed by the applicable Creative Commons License

electromechanical coupling coefficient. The system parameters for the fabricated physical prototype are listed in Table 1.

The free decay experiment is repeated 10 times under the same load resistance to ensure that the results are repeatable. The natural frequencies of the piezo-beam under different load resistances are obtained from the power spectrum analysis of the voltages across the load resistance, acquired by an oscilloscope. In the free decay experiment, the ratio of the sum of the adjacent peaks is defined as the attenuation coefficient as follows:

$$\varphi=\frac{|A_N|+|A_{N+1}|+|A_{N+2}|+\cdots|A_{N+n-1}|}{|A_{N+1}|+|A_{N+2}|+|A_{N+3}|+\cdots|A_{N+n}|}=e^{\pi\frac{\xi}{\sqrt{1-\xi^2}}}. \tag{22}$$

Then, the damping ratio can be determined by

$$\xi=\frac{0.733\lg\varphi}{\sqrt{1+(0.733\lg\varphi)^2}}=\frac{\lg\varphi}{\sqrt{1.862+(\lg\varphi)^2}}. \tag{23}$$

For the piezo-beam, the variations in the natural frequency and damping ratio with the increase of the load resistance can be obtained by using the linear analysis method.[33] The linear analytical results are compared with those from the free decay experiment, as shown in Figure 3. Both results are in consistent. The natural frequency first increases until the load resistance increases up to $R = 9\times10^5\Omega$ then keeps almost constant even R further increases larger than $9\times10^5\ \Omega$. The increase in the natural frequency is, however, small, less than 0.5%. With the increase of the load resistance, the effective damping ratio of the piezo-beam first increases then decreases and reaches the maximum of 0.03 at $R = 1.34\times10^5\Omega$. The electromechanical coupling coefficient is $\vartheta_{eq} = 1.725\times10^{-4}\mathrm{NV}^{-1}$ as follows[25]:

$$\vartheta_{eq}=\sqrt{k_{eq}C_p\left[\left(\frac{f_{oc}}{f_{sc}}\right)^2-1\right]}. \tag{24}$$

Here, $k_{eq} = 21.89Nm^{-1}$ represents the short-circuit stiffness of the piezo-beam; $f_{oc} = 7.828$ Hz and $f_{sc} = 7.789$ Hz represent, respectively, the natural frequencies under the open-circuit ($R = 5$ MΩ) and short-circuit ($R = 6.745$ kΩ) conditions.

The air flow within the wind tunnel is generated by a fan system, which is driven by a motor of 370 W. The stepless speed regulation is realized by using a frequency converter. The wind speed range lies between 2 and 12 m/s. The cross-section of the wind tunnel is $190\times190\ \mathrm{mm}^2$ and the length is 783 mm. The prototype is placed in the middle of the wind tunnel. A laser sensor is installed outside the wind tunnel, 200 mm away from the prototype to measure the displacement of the lower edge of the cylinder. The adopted laser displacement sensor is the Panasonic HG-C1200 model, which has the maximum range of −80 to 80 mm and a resolution of 0.01 mm. The voltage signals from the laser sensor and the load resistance are recorded by an oscilloscope.

Similarly, the natural frequency of the built-in cylinder system (including the piezo-beam) is measured as $f_n = 3.44$ Hz. The natural frequency of the cylinder only (ie, without the piezo-beam) is $f_c = 4.36$ Hz. The entire experimental setup and its installation are shown as Figure 4. In order to reduce the signal-to-noise ratio, the load resistance is set at 1 MΩ.

Figure 5A-D shows the time histories and power spectrum of the cylinder displacement under different reduced

TABLE 1 The system parameters for the proposed flow-induced PEH

Parameter	Description	Piezoelectric layer (PZT-5H)	Substrate (Cu)	Tip mass	Cylinder
L_p, L_s, L_t, L_c	Length (mm)	30	90	5	130
b_p, b_s, b_t	Width (mm)	15	15	15	—
h_p, h_s, h_t	Thickness (mm)	0.2	0.2	5	—
D	Diameter (mm)	—	—	—	52
ρ_p, ρ_s	Density (kg/m^3)	7600	8900	—	—
m_p, m_s, m_t, m_c	Weight (g)	1.37	2.70	8.65	16.50
d_{31}	Piezoelectric constant (10^{-12} C/N)	550	—	—	—
$\bar{\varepsilon}_{33}^{S}$	Dielectric constant (nF/m)	30.1	—		—
C_p	Capacity (nF)	135.4	—		—

Abbreviation: PEH, piezoelectric energy harvester.

1099114x, 2020, 5, Downloaded from https://onlinelibrary.wiley.com/doi/10.1002/er.5164 by The Hong Kong University Of Science & Technology, Wiley Online Library on [17/04/2026]. See the Terms and Conditions (https://onlinelibrary.wiley.com/terms-and-conditions) on Wiley Online Library for rules of use; OA articles are governed by the applicable Creative Commons License

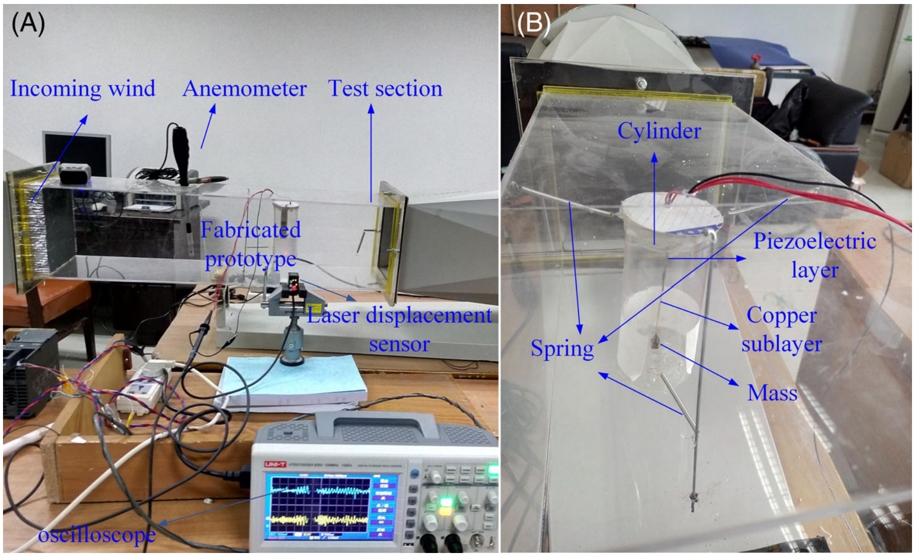

FIGURE 4 Experimental setup. A, Photograph of the experimental facilities; B, close-up view of the energy harvester [Colour figure can be viewed at wileyonlinelibrary.com]

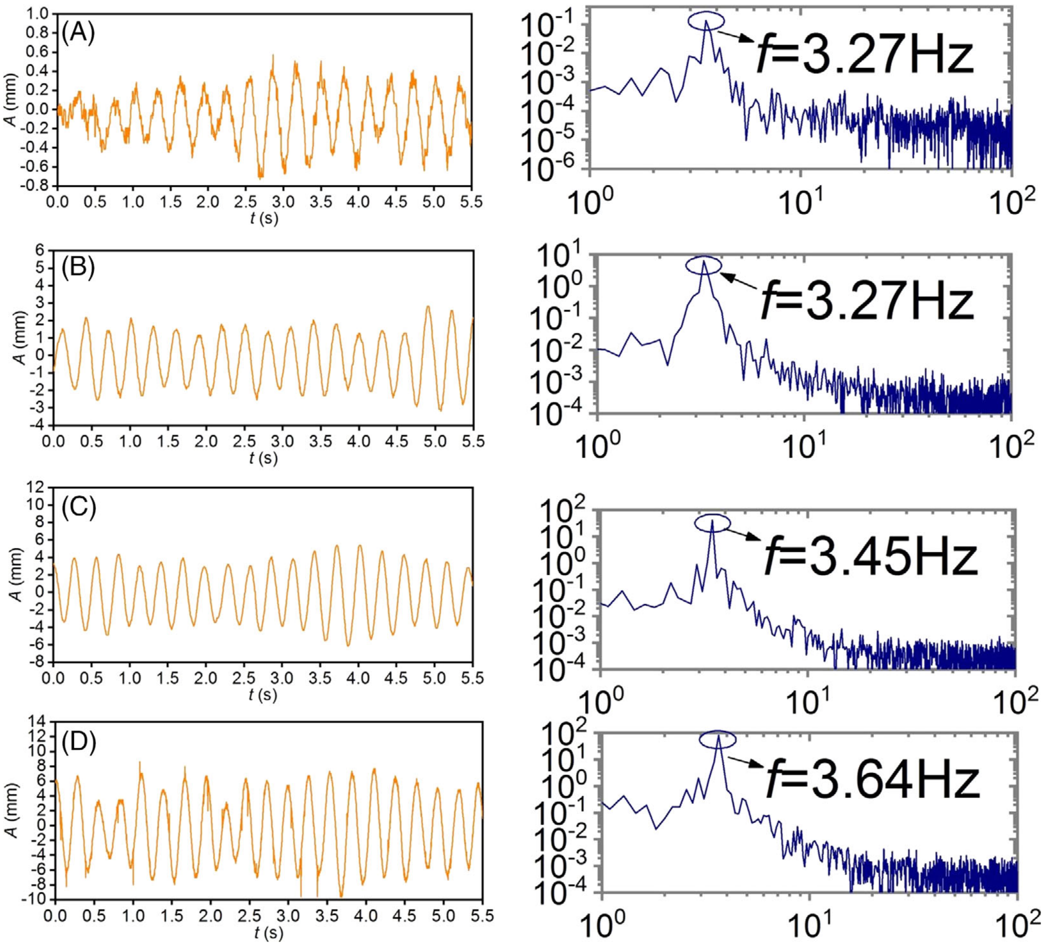

FIGURE 5 Time-histories of the cylinder displacement and the corresponding frequency spectra for (A) $U^* = 21.80$, (B) $U^* = 38.01$, (C) $U^* = 46.96$, and (D) $U^* = 65.97$ [Colour figure can be viewed at wileyonlinelibrary.com]

velocity $U^*(U^* = U/f_nD)$ of wind. The corresponding vibration frequencies under four wind velocities are $f_c \approx 3.27$Hz, $f_c \approx 3.27$Hz, $f_c \approx 3.45$Hz, and $f_c \approx 3.64$Hz, respectively. For the reduced velocities in Figure 5, the natural vortex shedding frequency (fixed cylinder) is about 16, 28, 35, and 48 Hz, respectively, which are much higher than the natural frequency (ie, $f_n = 3.44$ Hz) of the cylinder system. The entire system thus performs a self-excited

1099114x, 2020, 5, Downloaded from https://onlinelibrary.wiley.com/doi/10.1002/er.5164 by The Hong Kong University Of Science & Technology, Wiley Online Library on [17/04/2026]. See the Terms and Conditions (https://onlinelibrary.wiley.com/terms-and-conditions) on Wiley Online Library for rules of use; OA articles are governed by the applicable Creative Commons License

oscillation. The vibration mechanism and phenomenon are very similar to those of the galloping vibration. There are three reasons to identify why it is galloping. First, the vibration frequency is close to the natural frequency of the cylinder. Second, the vibration amplitude increases with increasing *U**. Third, the natural vortex shedding frequency is much higher (4.5-14 times) than the vibration frequency. All these indicate galloping vibration.

Figure 6A-D shows the time-histories and power spectrum of the output voltage under different *U**. The response of the output voltage is more complex than that of the cylinder displacement. As can be seen in Figure 6A, the output voltage is low when the wind speed is $U^* = 21.80$. The corresponding power spectrum displays three peaks at $f_{V1} \approx 3.27$, $f_{V2} \approx 8.91$, and $f_{V3} \approx 16.18$ Hz, respectively. Obviously, f_{V1} is the vibration frequency of the external cylinder. f_{V2} is close to the natural frequency of the piezo-beam, while f_{V3} is close to the natural vortex shedding frequency of the external cylinder. Thus, the excitation involves the external cylinder vibration, vortex shedding, and piezoelectric-beam inertial force. Note that the amplitudes of the output voltage and cylinder displacement are low, f_{V3} is thus close to the vortex shedding frequency. This may not be the case when the amplitude is high. When U^* is increased to 38.01 (the case in Figure 6B), the output voltage is increased. The frequency spectrum are unchanged, that is, $f_{V1} \approx 3.27$, $f_{V2} \approx 8.18$, and $f_{V3} \approx 9.27$ Hz. As the vibration amplitude continues to increase, the oscillation of the external cylinder will have a greater influence. Therefore, the vibration frequency of the external cylinder becomes the dominant frequency of the output voltage. As can be noted in Figure 6C, the output voltage monotonically increases when U^* is increased up to 46.96. Under this case, there are only two peaks in the frequency spectrum, that is, $f_{V1} \approx 3.45$ and $f_{V2} \approx 8.73$ Hz. And, the vibration frequency of the external cylinder is still dominant. For the case presented in Figure 6D, the result at $U^* = 65.97$ is similar to that at the wind speed of $U^* = 46.96$ and the two frequency peaks change slightly, that is, $f_{V1} \approx 3.64$ Hz and $f_{V2} \approx 8.36$ Hz.

Figure 7A-C shows the variations in the mean cylinder displacement amplitude, mean output voltage amplitude, and corresponding power as *U** increases. Both displacement and output voltage amplitudes increase with the increase of *U**, as well for the average power. When $U^* \leq 40$, the increase rates of these three quantities are small. However, their increase rates are high when U^* is greater than 40. At the largest wind speed (ie, $U^* = 65.97$) examined, the displacement amplitude, output voltage, and average power are, respectively, $A_{max} = 7.66$ mm, $V_{max} = 3.391$ V, and $P_{avg} = 5.75$ μW. It is worth mentioning that the impedance matching in the experiment was not attained, so the actual optimal power could be larger than 5.75 μW.

Figure 7D presents the dominant frequency of the output voltage response and evolution of the cylinder vibration frequency as *U** increases. When $U^* \leq 21.80$, the two dominant frequencies are not the same. In addition, the dominant frequency of the output voltage is the same as the vortex shedding frequency and the vibration frequency of the cylinder is close to the natural frequency

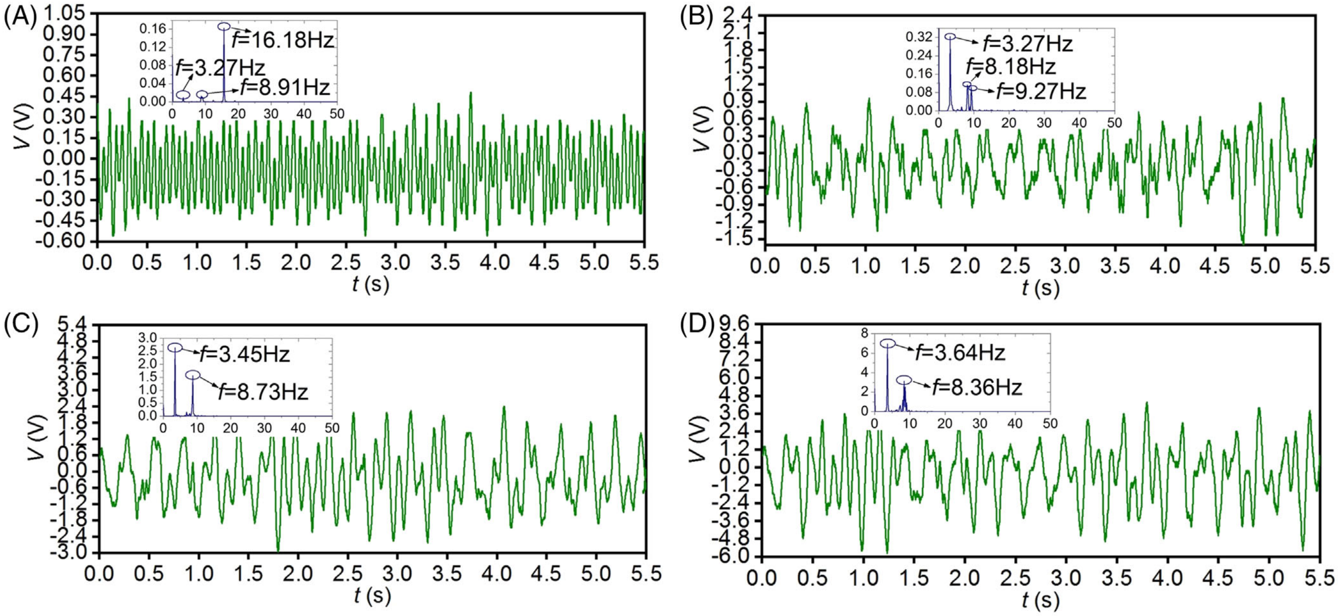

FIGURE 6 Time-histories of the voltage output of the proposed vortex-induced vibration (VIV)-piezoelectric energy harvester (PEH) and the corresponding frequency spectra for (A) $U^* = 21.80$, (B) $U^* = 38.01$, (C) $U^* = 46.96$, and (D) $U^* = 65.97$ [Colour figure can be viewed at wileyonlinelibrary.com]

1099114x, 2020, 5, Downloaded from https://onlinelibrary.wiley.com/doi/10.1002/er.5164 by The Hong Kong University Of Science & Technology, Wiley Online Library on [17/04/2026]. See the Terms and Conditions (https://onlinelibrary.wiley.com/terms-and-conditions) on Wiley Online Library for rules of use; OA articles are governed by the applicable Creative Commons License

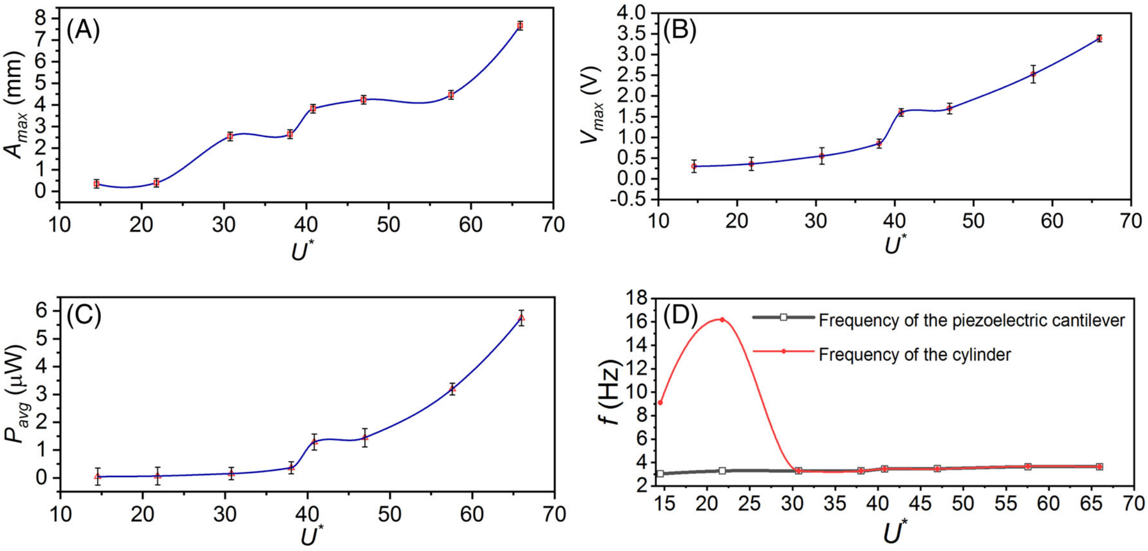

FIGURE 7 The responses of the vortex-induced vibration (VIV)-piezoelectric energy harvester (PEH) to different wind speeds: (A) displacement amplitude, (B) output voltage amplitude, (C) power output, and (D) predominant frequencies [Colour figure can be viewed at wileyonlinelibrary.com]

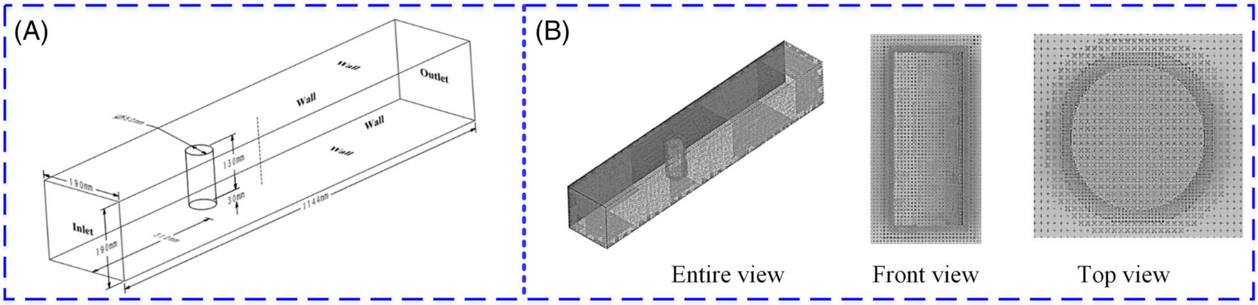

FIGURE 8 A, The computational domain; B, comprehensive views of the grids near the cylinder [Colour figure can be viewed at wileyonlinelibrary.com]

of the piezo-beam. Moreover, with the increase of U^*, the dominant frequency of the output voltage synchronizes with the vibration frequency of the cylinder.

4 | NUMERICAL SIMULATION OF FLUID-STRUCTURE INTERACTION

A coupled fluid-structure electrical model of the proposed VIV-PEH is established using the lattice Boltzmann method (LBM). Different from traditional CFD methods, instead of solving the Navier-Stokes equations directly, LBM simulates the macroscopic behaviour of fluids by using a simple mesoscopic model. LBM is increasingly attracting researchers from the field of computational physics in recent years for several advantages, such as in dealing with complex geometric boundaries. More details of LBM, especially its application for FSI problems, can be referred to previous studies.[39-41] Since the LBM theory is not the focus of this study, the commercial software XFlow that uses LBM technology is employed for conducting the following simulation.[42] In order to make the results be comparable with those from the above experiment, we take the same system parameters for the wind tunnel experiment in the simulation. The cross-section of the computational domain is also the same as that of the wind tunnel, except that its length is extended appropriately (Figure 8A). The left and right boundaries are, respectively, defined as the flow inlet and outlet, and the remaining boundaries are set as walls. The wall-adapting local eddy-viscosity model (which is a large eddy simulation turbulence model) provided by XFlow is used to simulate the flow with a Reynolds number ranges from 8400 to 42 000. To verify the convergence of lattice size in the numerical calculation by using the LBM, 3D flow around a fixed cylinder is firstly conducted for $U^* = 13.98$ ($U = 2.4$ m/s). Three different grid sizes are employed. The size of the far-field grid used here is four times that

1099114x, 2020, 5, Downloaded from https://onlinelibrary.wiley.com/doi/10.1002/er.5164 by The Hong Kong University Of Science & Technology, Wiley Online Library on [17/04/2026]. See the Terms and Conditions (https://onlinelibrary.wiley.com/terms-and-conditions) on Wiley Online Library for rules of use; OA articles are governed by the applicable Creative Commons License

of the near-wall grid. Three different grid densities (ie, 0.025D, 0.0125D, and 0.00625D) near the cylinder are tested. In the calculation, *Courant* = 1 is set to automatically adjust the time step. Table 2 lists the corresponding amplitudes for the lift coefficient C_L, drag coefficient C_D, and Strouhal number S_t. Figure 9 shows the time histories of the drag force for the coarse, medium, and fine meshes. It can be seen that the results are gradually converged, with the maximum deviation declining. To balance the trade-off between the computational expense and accuracy, we adopt the medium mesh density for the following simulations. The total number of elements is 3 067 040. The entire calculation domain and grids in the area near the cylinder wall are shown in Figure 8B.

4.1 | Comparison between numerical and experimental results

The results from the numerical simulation and experiment for the mean displacement amplitude and the vibration frequency of the cylinder are compared in Figure 10A,B, respectively. It is found that the intensive vibration of the cylinder in the experiment begins earlier, this may be due to the flow disturbance by supporting wire and springs. It is worth noting that although the numerical simulation did not consider the presence of springs in the flow domain, the results from the simulation and experiment are reasonably in consistent with each other. Figure 10A,D compares the voltage output and dominant frequencies obtained from the numerical simulation and experiment. In terms of the output voltage, it is noted that the numerical calculation result is very close to that from the experiment for $U^* < 40$ but the former is lower than the latter for $U^* > 40$. This is because, when the power is experimentally produced through piezoelectric system, there may be a system loss in the power production process. Also, the bonding of the piezo-beam to the cylinder cap made of cardboard cannot be perfect in the experiment. In addition, the rigidity of the cardboard is not infinite. It can dissipate some energy, affecting the output voltage. The piezo-beam is rigidly connected to the cylinder cap in in the mathematical model. However, the variation trend of the output voltage as the wind speed changes is in consistent with the experimental results within the wind speed range. As to the dominant frequencies of the output voltage, the numerical result agrees well with the experimental result when $U^* > 35$. But for small U^*, the high-frequency vibration of the piezo-beam is not captured in the simulation, which is slightly different from the experimental result. The explanation may be that since the piezo-beam is simplified as a single-degree-of-freedom (SDOF) system and the high-order modes are not considered in the numerical modelling, the resonance generated by the vortex shedding frequency, and the high-order modes are

TABLE 2 The mesh convergence study results ($U = 2.4$ m/s)

Mesh	C_L	C_D	S_t
Coarse	0.601	1.189	0.188
Medium	0.623 (3.66%)	1.202 (1.09%)	0.197 (4.79%)
Fine	0.631 (1.28%)	1.209 (0.28%)	0.202 (2.54%)

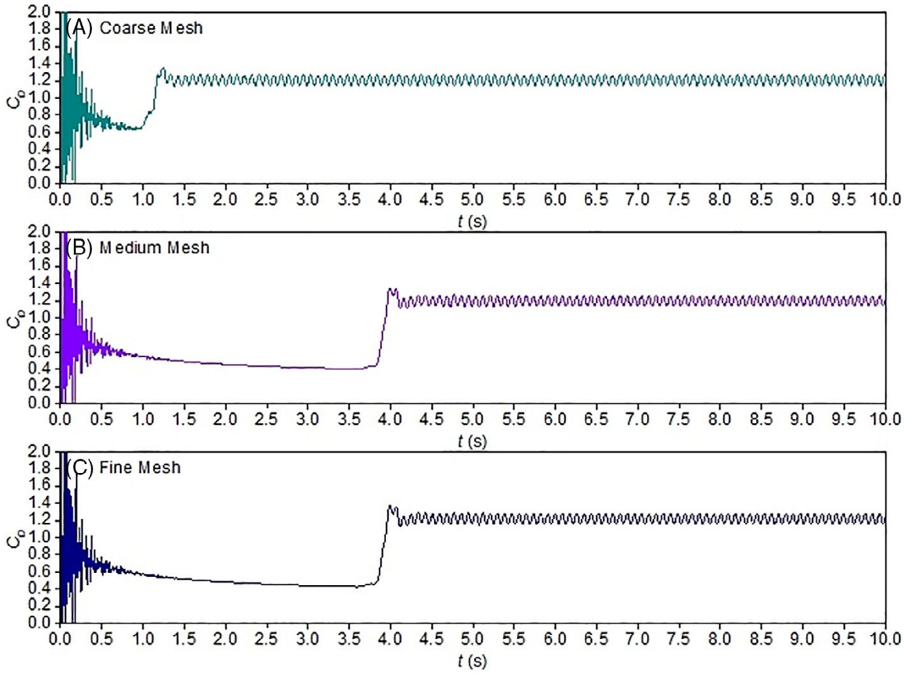

FIGURE 9 Time histories of drag force for (A) coarse, (B) medium, and (C) fine meshes [Colour figure can be viewed at wileyonlinelibrary.com]

1099114x, 2020, 5, Downloaded from https://onlinelibrary.wiley.com/doi/10.1002/er.5164 by The Hong Kong University Of Science & Technology, Wiley Online Library on [17/04/2026]. See the Terms and Conditions (https://onlinelibrary.wiley.com/terms-and-conditions) on Wiley Online Library for rules of use; OA articles are governed by the applicable Creative Commons License

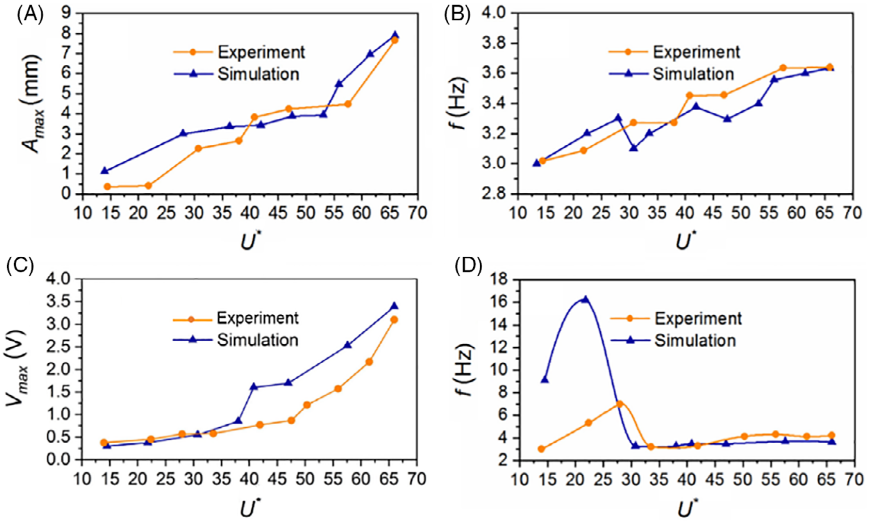

FIGURE 10 Comparison between the simulation and the experiment results: A, mean displacement amplitude of the cylinder; B, cylinder vibration frequency; C, harvested voltage output; and D, frequencies of voltage output [Colour figure can be viewed at wileyonlinelibrary.com]

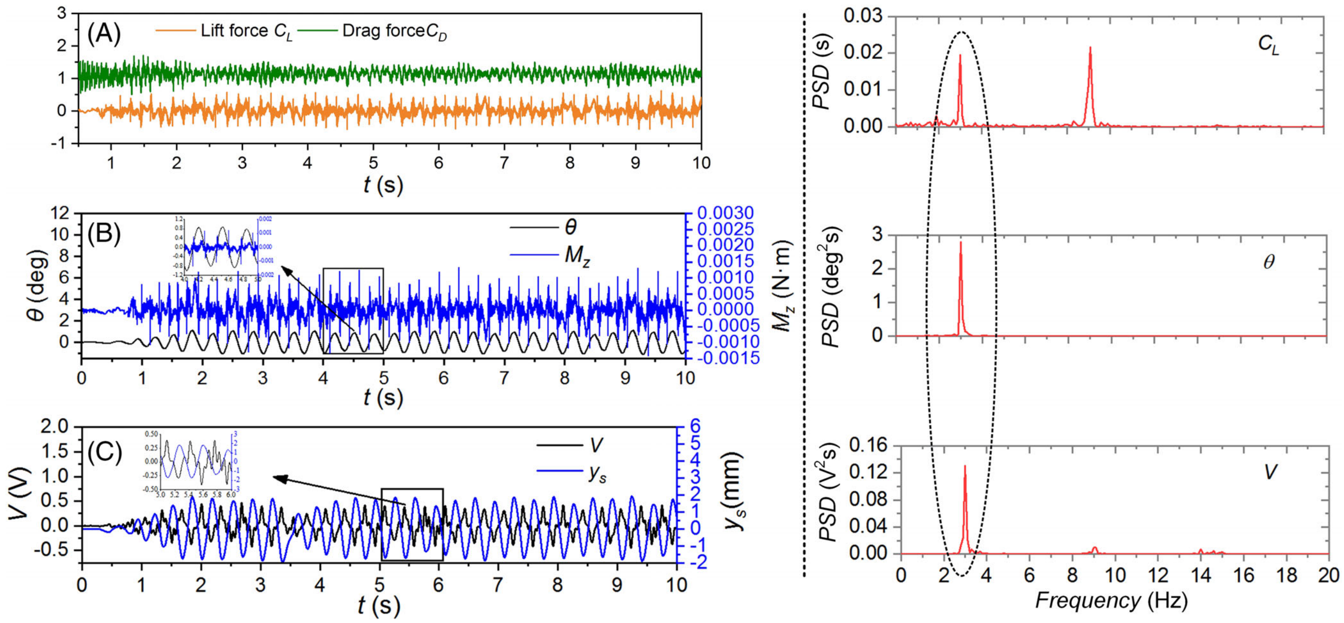

FIGURE 11 The main parametric output from the numerical simulation for $U^* = 13.98$. A, Time-histories of C_L and C_D; B, swing angle and torque on the cylinder; C, harvested voltage and tip displacement; D, power spectrum of C_L, θ, V [Colour figure can be viewed at wileyonlinelibrary.com]

thus not captured. In addition, the displacement amplitude is slightly larger than that measured in the experiment under the low wind speed, which has a significant influence on the flow field, resulting in the change of the vortex shedding frequency. The forced vibration of the piezo-beam is therefore mainly affected by the vortex-shedding process. The system vibrates at its natural frequency as the displacement amplitude of the cylinder increases. Both simulation and experiment studies demonstrate that the dominant frequency of the output voltage is close to the natural frequency.

4.2 | Discussions on the numerical results

The simulated results are presented in Figure 11 for different parameters. The variation in lift is basically sinusoidal with an amplitude of $C_L \approx 0.6$, while the average drag coefficient is $C_D \approx 1.2$ for the entire cylinder (Figure 11A). As noted from Figure 11B, the time-history of the cylinder pendulum angle obviously shows that the cylinder oscillation is sinusoidal. However, the torque pulsation is relatively strong and its spectral components

1099114x, 2020, 5, Downloaded from https://onlinelibrary.wiley.com/doi/10.1002/er.5164 by The Hong Kong University Of Science & Technology, Wiley Online Library on [17/04/2026]. See the Terms and Conditions (https://onlinelibrary.wiley.com/terms-and-conditions) on Wiley Online Library for rules of use; OA articles are governed by the applicable Creative Commons License

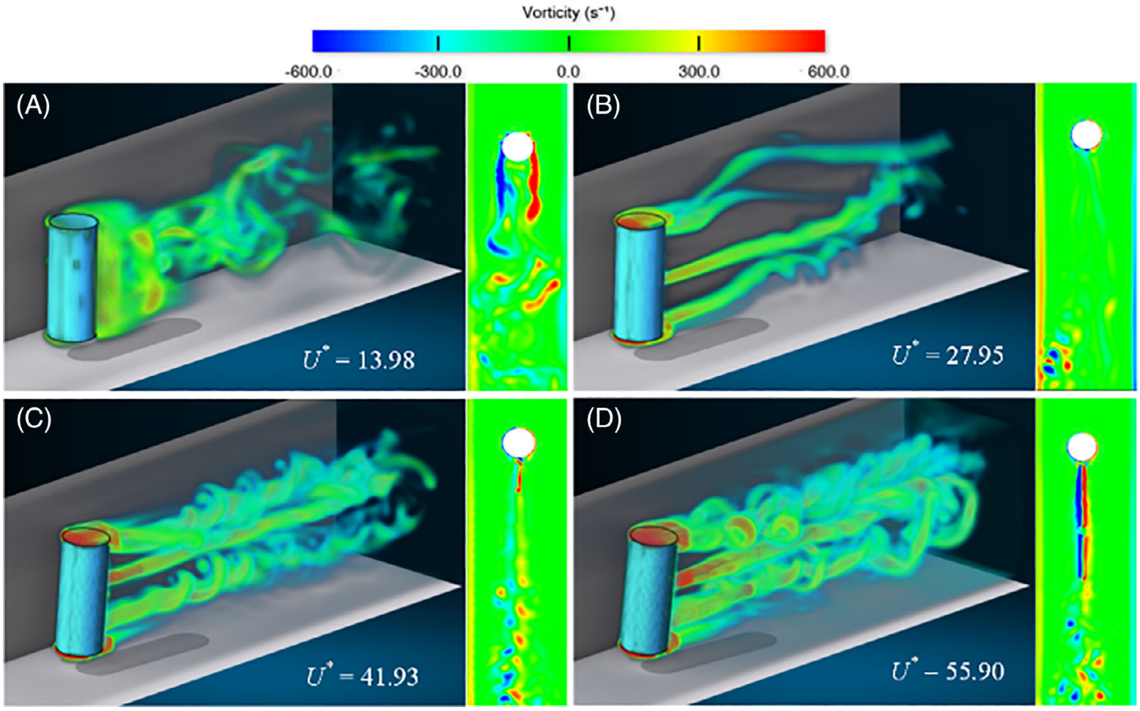

FIGURE 12 The vorticity contours of the flow field: (A) $U^* = 13.98$, (B) $U^* = 27.95$, (C) $U^* = 41.93$, and (D) $U^* = 55.90$ [Colour figure can be viewed at wileyonlinelibrary.com]

are complex. According to Figure 11C, the response of the output voltage and displacement of the piezo-beam are basically opposite. The spectra of the lift coefficient C_L, the cylinder pendulum angle θ, and the output voltage V are shown in Figure 11D, from which we can see that the responses of θ and output voltage V have the same dominant frequency which is close to the natural frequency of the piezo-beam. There are two high-frequency peaks in the lift power spectrum. The first one corresponds to the cylinder vibration frequency, and the other corresponds to the vortex-shedding frequency. However, although there are two peaks in the lift force power spectrum, the natural frequency of the cylinder is quite different from the vortex-shedding frequency. The vibration response of the cylinder has thus no frequency component close to the vortex-shedding frequency. The cylinder is thus under a state of self-excited vibration. From the spectral analysis of the output voltage, we can see that there are higher-frequency components close to the natural frequency and the vortex-shedding frequency of the cylinder, which shows that the piezo-beam is subjected to the forced vibration under the excitation of the cylinder, and on the other hand, the natural frequency of the piezo-beam is close to the vortex-shedding frequency in this case. Moreover, there are also higher-frequency components near to the vortex-shedding frequency. This phenomenon is also observed in the experiment.

Figure 12 shows the 3D vorticity cloud diagram for $U^* = 13.98$, 26.4, 41.93, and 55.90, and the plane vorticity cloud diagram at the mid-section of the cylinder when the cylinder is at its maximum displacement. With the increase of the wind speed, the displacement amplitude, the vorticity pattern varies significantly. When $U^* = 13.98$, the formation of vortices takes place near the cylinder, with vortices dissipating gradually during their convection downstream. As the wind speed increases, especially when it is up to $U^* = 26.4$, the increased cylinder vibration amplitude significantly affects the flow field. Although the obvious vortex shedding is not observed near the cylinder, some streamwise vorticity bands and visible vortices in the far wake are discernible (see both 3D and 2D snapshots). For $U^* = 41.93$ or 55.90, the reconstruction of the vortex shedding starts, with obvious vortex shedding identified in the 3D figure. In the 2D figure, although the obvious vortices are not discernible near the cylinder, the vortices in the far wake are significantly enhanced. In short, the swing of the cylinder has a great influence on the flow field and the vortex shedding from the cylinder differs from that from nearly fixed cylinder (low amplitude). In addition, the formation and evolution of vortices in the wake are very complex. The lift force frequency cannot be simply understood as the vortex shedding frequency when the cylinder oscillates.

1099114x, 2020, 5, Downloaded from https://onlinelibrary.wiley.com/doi/10.1002/er.5164 by The Hong Kong University Of Science & Technology, Wiley Online Library on [17/04/2026]. See the Terms and Conditions (https://onlinelibrary.wiley.com/terms-and-conditions) on Wiley Online Library for rules of use; OA articles are governed by the applicable Creative Commons License

5 | THEORETICAL ANALYSIS AND DISCUSSIONS

5.1 | Verification of the theoretical model

On the basis of comparing and analysing the experimental and numerical results, this section improves the theoretical modelling for the proposed flow-induced vibration energy harvester. As to the theoretical model, the key to determine the aerodynamic parameters lies in identifying the lift and drag coefficients and its frequency. We make the following assumptions to simplify the parameter identification process:

Assumption 1: The external cylinder is rigid, and the influence of the elastic deformation when connecting it with the piezo-beam is ignored.

Assumption 2: The swing of the device has an effect on the aerodynamic force that is similar to the relationship between the acting force and the reaction force. The excitation frequency is the same as the natural frequency of the coupled system.

Assumption 3: The lift and drag coefficients remain unchanged across the cylinder in the considered wind speed range.

Assumption 4: The lift coefficient changes sinusoidally with time.

According to the above assumptions, the identified lift coefficients are $C_L = 0.6$ and $C_D = 1.2$. Since the lift force is a sinusoidal function of time, it can thus be expressed as

$$C_L(t) = C_L \sin(2\pi f_n t). \tag{25}$$

Here, f_n is the natural frequency of the coupled system when implementing the piezo-beam within the cylinder. After installing the piezo-beam, the free vibration attenuation experiment is performed by pulling the cylinder to a small angle and then measuring the swing amplitude at the lower edge of the cylinder. In the theoretical equation, this frequency needs to be considered for the restoring torque provided by the equivalent mass of the piezo-beam. Thus,

$$f_n = \frac{m_c g L_c + 2k_y L_c^2 + 2m_{eq} g L_s}{4\pi J_{total}}. \tag{26}$$

Here, $k_y = 3.757\text{N/m}$ and $J_{total} = J_z + m_{eq} L_s^2$. By substituting Equation (25) into Equation (21) and combining Equations (2) to (4), a complete theoretical model of the built-in PEH can be developed.

Figure 13A compares the theoretical and experimental results of the cylinder swing angle amplitude, from which we find that the theoretical results are in consistent with the experimental results in the considered wind speed range. Figure 13B compares the theoretical and experimental results of the output voltage amplitude. As expected, both the results are well in consistent with each other. Therefore, we can conclude that the experiment proves the accuracy of the theoretical model of the proposed flow-induced vibration energy harvester.

5.2 | Parametric study

Based on the developed theoretical model, further analysis is performed to understand the effects of the system parameters on the performance of the proposed flow-induced vibration energy harvester. First, the effect of the

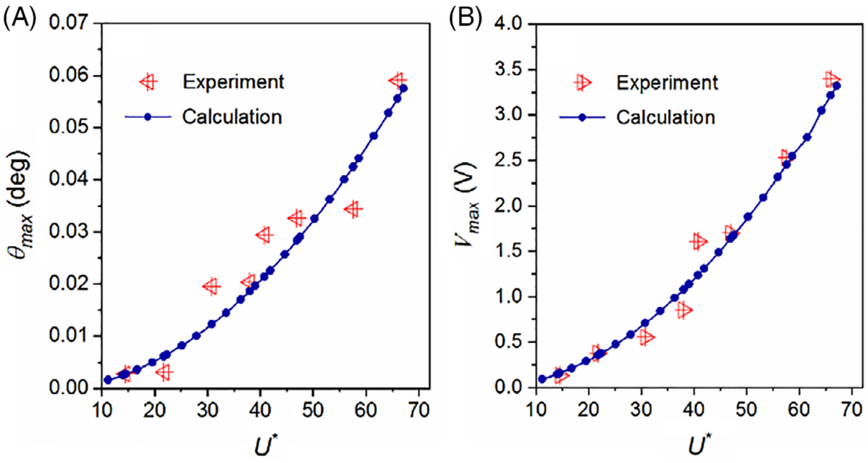

FIGURE 13 The comparison between (A) oscillation angles, and (B) the harvested voltages obtained from the theoretical calculation and experiment [Colour figure can be viewed at wileyonlinelibrary.com]

1099114x, 2020, 5, Downloaded from https://onlinelibrary.wiley.com/doi/10.1002/er.5164 by The Hong Kong University Of Science & Technology, Wiley Online Library on [17/04/2026]. See the Terms and Conditions (https://onlinelibrary.wiley.com/terms-and-conditions) on Wiley Online Library for rules of use; OA articles are governed by the applicable Creative Commons License

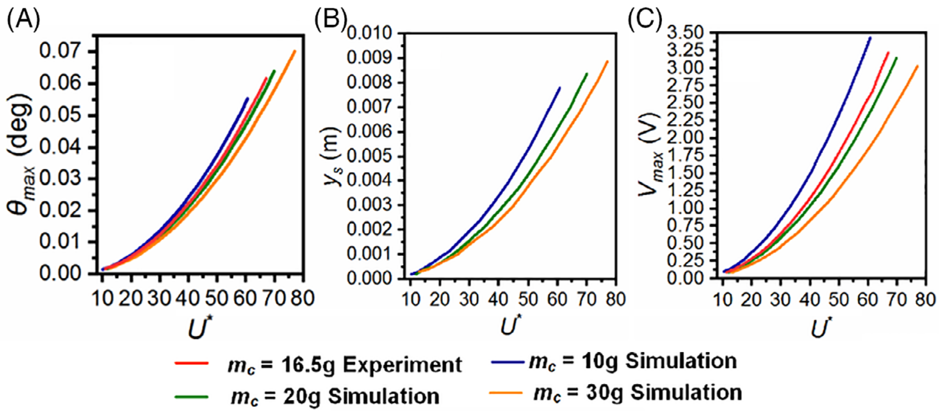

FIGURE 14 Variations in (A) the cylinder amplitude, (B) tip mass displacement, and (C) harvested voltage under different cylinder masses [Colour figure can be viewed at wileyonlinelibrary.com]

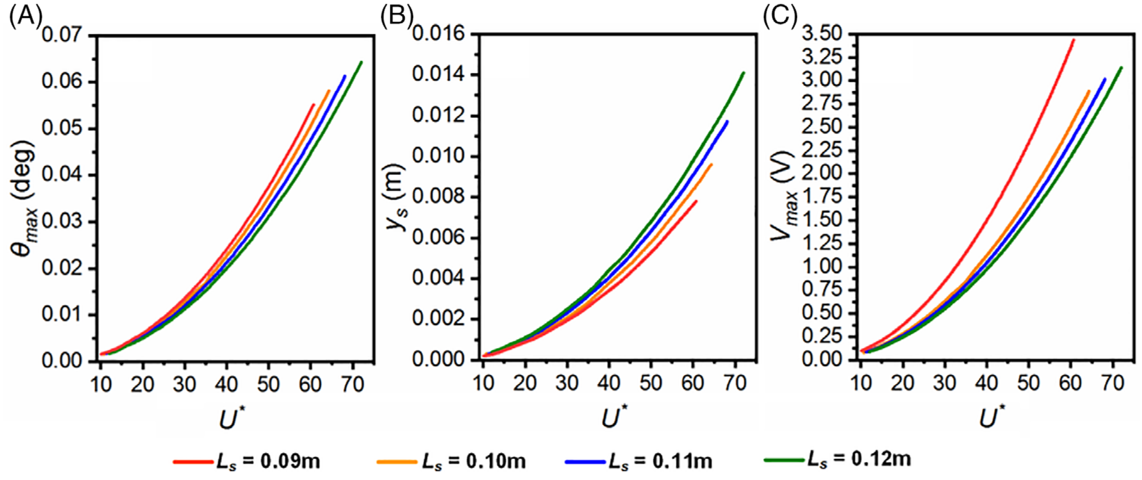

FIGURE 15 Variations in (A) cylinder amplitude, (B) tip mass displacement, and (C) harvested voltage for different lengths of the piezo-beam [Colour figure can be viewed at wileyonlinelibrary.com]

cylinder mass is analysed for three different m_c, that is, 10, 20, and 30 g. The corresponding natural frequencies of the three systems are respectively 3.80, 3.30, and 3.00 Hz. The calculated and experimental ranges of the wind speed are $10 < U^* < 80$ and 2 m/s $< U <$ 12 m/s, respectively.

For different cylinder mass m_c, that is, 10, 20, and 30 g, Figure 14 shows the variations of the cylinder swing angle amplitude, the displacement amplitude at the free end of the piezo-beam, and the output voltage with an increase in the wind speed U^*. The swing angle amplitude increases with the decrease of m_c, regardless of the wind speed. It is also true for the displacement amplitude and the output voltage. This phenomenon is associated with the three-degree-of-freedom characteristic of the coupled system. With the decrease of the cylinder mass, the natural frequencies of the cylinder and coupled system increase due to the installation of the piezo-beam. Since the internal piezo-beam is unchanged, the vibration frequency of the energy harvester is closer to the natural frequency of the piezo-beam. In addition, a decrease in the cylinder mass reduces the mass ratio of the whole system while increases the vibration amplitude. Consequently, much more wind energy is converted into electricity during the vibrations of the cylinder and piezo-beam.

The influence of the total length of the cantilever beam on the performance of the energy harvester is revealed in Figure 15. For the given cylinder mass $m_c = 10$ g, three cases with $L_s = 100$, 110, and 120 mm are analysed. The corresponding natural frequencies of the coupled system are 3.59, 3.39, and 3.21 Hz, respectively.

Figure 15 presents the effects of the piezo-beam length on the cylinder swing angle amplitude, displacement amplitude at the free end of the piezo-beam, and output voltage. Figure 15A demonstrates that the swing angle amplitude of the cylinder decreases with the increase of the piezo-beam length, which agrees with the variation tendency of the voltage output (Figure 15C). However, an opposite scenario is observed for the

1099114x, 2020, 5, Downloaded from https://onlinelibrary.wiley.com/doi/10.1002/er.5164 by The Hong Kong University Of Science & Technology, Wiley Online Library on [17/04/2026]. See the Terms and Conditions (https://onlinelibrary.wiley.com/terms-and-conditions) on Wiley Online Library for rules of use; OA articles are governed by the applicable Creative Commons License

displacement amplitude (Figure 15B) and an increase in the beam length leads to an increase in the displacement amplitude. This is because the mass ratio of the entire harvesting system increases with the increase of the beam length, while the equivalent stiffness and the natural frequency of the beam become smaller. The relationship between the output voltage amplitude and beam length is similar to that between the swing amplitude and beam length. The reason behind the decrease in the output voltage amplitude is that the electromechanical coupling coefficient becomes smaller when the length of the beam increases. However, the natural frequency of the piezo-beam also decreases at the same time and gets closer to the natural frequency of the energy harvester. That is, the entire system approaches the resonance state. The change in the vibration frequency compensates in a certain extent the effect of the decreasing electromechanical coupling coefficient. Therefore, although all the output voltage levels for $L_z > 0.09$ are lower than those for $L_s = 0.09$ m, the decline rate of the output voltage is lower for larger L_z.

From the above discussions, we know that the relationships between the system parameters of the proposed flow-induced vibration energy harvester and its operating performance are extremely complicated nonlinear. Variations in both mass of the external cylinder and length of the piezo-beam have effects on the energy conversion efficiency. And, reducing the mass of the external cylinder can directly increase the output voltage amplitude.

NOMENCLATURE

b_p, b_s, b_t	width of the piezoelectric layer, substrate, tip mass
c	damping coefficient
c_{eq}	equivalent damping coefficient
C_L, C_D	lift coefficient, drag coefficient
C_p	clamped capacitance of the piezoelectric transducer
d_{31}	piezoelectric constant
D	diameter of the cylinder
f_{oc}, f_{sc}	natural frequency under open-circuit condition, short-circuit condition
I_p	inertia moment
J_z	moment of inertia
k_y	y-direction component of the stiffness of the front spring
k_{eq}	equivalent stiffness
m_c	cylinder mass
m_{eq}	equivalent mass
L_p, L_s, L_t, L_c	length of the piezoelectric layer, substrate beam, tip mass, cylinder
M	moment of the transverse force
R	load resistance
U	wind speed
V	voltage generated by the piezoelectric transducer
y_s	the piezo-beam displacement at the free end
α	attack angle
μ_1	correction coefficient
ω_n	natural frequency of the compound pendulum
ϑ_{eq}	equivalent electromechanical coupling coefficient
$\bar{\varepsilon}_{33}^S$	dielectric constant
ρ_p, ρ_s	mass density of piezoelectric material, substrate material
θ	pendulum swing angle
ξ	damping ratio

6 | CONCLUSIONS

The paper proposes a novel flow-induced vibration PEH consisting of a hollow cylinder and a built-in piezo-beam. A three-degree-of-freedom electromechanical coupled model is built by regarding the outer hollow cylinder as a compound pendulum and integrating with the lumped parameter model of the piezo-beam. Subsequently, a physical prototype is fabricated and a wind tunnel experiment is performed to test its real performance. From the experiment, the output characteristics of the energy harvester is analysed when the wind speed is increased. The results reveal that the output voltage increases with the increase of the wind speed. The vibration frequency of the energy harvester is relatively constant. After that, based on the experimental research and the numerical modelling, a parameter identification method to determine the lift coefficient and frequency for the theoretical model has been proposed. A good agreement is found between the theoretically calculated results and the experimental results. Therefore, the theoretical model can be used as a phenomenon-level model to perform a calculation for this type of energy harvester. It is discovered that a decrease in the cylinder mass can improve the energy-harvesting efficiency. Moreover, decreasing the piezo-beam length can increase the voltage output.

The main advantage of this proposed design is that there are no direct interactions between the piezo-beam and the flow. Besides this, the outer hollow cylinder can provide protection for the piezo-beam. In a practical working environment, especially underwater, the piezoelectric layer can be protected from external debris and corrosion. Rather than insulating the piezo-beam, it simply seals the cylinder. In summary, the proposed energy harvester presented in the paper is capable of energy harvesting. However, the approaches for improving its

1099114x, 2020, 5, Downloaded from https://onlinelibrary.wiley.com/doi/10.1002/er.5164 by The Hong Kong University Of Science & Technology, Wiley Online Library on [17/04/2026]. See the Terms and Conditions (https://onlinelibrary.wiley.com/terms-and-conditions) on Wiley Online Library for rules of use; OA articles are governed by the applicable Creative Commons License

energy-harvesting performance are worth being further explored.

ACKNOWLEDGEMENT

This work is supported by the National Natural Science Foundation of China (grants 51606171 and 51977196).

ORCID

Min Zhang https://orcid.org/0000-0003-0377-803X
Guobiao Hu https://orcid.org/0000-0002-1288-7564

REFERENCES

1. Fan K, Liang G, Zhang Y, Tan Q. Hybridizing linear and nonlinear couplings for constructing two-degree-of-freedom electromagnetic energy harvesters. *Int J Energy Res*. 2019;43(14):8004-8019.
2. Liu W, Yuan Z, Zhang S, Zhu Q. Enhanced broadband generator of dual buckled beams with simultaneous translational and torsional coupling. *Appl Energy*. 2019;251:113412.
3. Hu G, Wang J, Su Z, Li G, Peng H, Kwok K. Performance evaluation of twin piezoelectric wind energy harvesters under mutual interference. *Appl Phys Lett*. 2019;115(7):073901.
4. Wang J, Tang L, Zhao L, Zhang Z. Efficiency investigation on energy harvesting from airflows in HVAC system based on galloping of isosceles triangle sectioned bluff bodies. *Energy*. 2019;172:1066-1078.
5. Liu W, Badel A, Formosa F, Zhu Q, Zhao C, Hu G-D. A comprehensive analysis and modeling of the self-powered synchronous switching harvesting circuit with electronic breakers. *IEEE Trans Ind Electr*. 2017;65(5):3899-3909.
6. Amini Y, Fatehi P, Heshmati M, Parandvar H. Time domain and frequency domain analysis of functionally graded piezoelectric harvesters subjected to random vibration: finite element modeling. *Compos Struct*. 2016;136:384-393.
7. Amini Y, Heshmati M, Fatehi P, Habibi S. Energy harvesting from vibrations of a functionally graded beam due to moving loads and moving masses. *J Eng Mech*. 2017;143(9):04017063.
8. Zhao L. Small-scale wind energy harvesting using piezoelectric materials, in School of Civil and Environmental Engineering. Nanyang Technological University; 2015.
9. Zou H-X, Zhao L-C, Gao Q-H, et al. Mechanical modulations for enhancing energy harvesting: principles, methods and applications. *Appl Energy*. 2019;255:113871.
10. Zhou S, Hobeck JD, Cao J, Inman DJ. Analytical and experimental investigation of flexible longitudinal zigzag structures for enhanced multi-directional energy harvesting. *Smart Mater Struct*. 2017;26(3):035008.
11. Tang L, Yang Y, Soh CK. Broadband vibration energy harvesting techniques. In: Elvin N et al., eds. *Advances in Energy Harvesting Methods*. New York, NY: Springer New York; 2013:17-61.
12. Zhou S, Cao J, Inman DJ, Jing L, Liu S, Wang Z. Broadband tristable energy harvester: modeling and experiment verification. *Appl Energy*. 2014;133(1):33-39.
13. Zhou S, Cao J, Inman DJ, Liu S, Wei W, Jing L. Impact-induced high-energy orbits of nonlinear energy harvesters. *Appl Phys Lett*. 2015;106(9):49-58.
14. Zhou S, Lei Z. Nonlinear dynamic analysis of asymmetric tristable energy harvesters for enhanced energy harvesting. *Commun Nonlinear Sci Numer Simula*. 2018;61:271-284.
15. Yang K, Fei F, Du J. Investigation of the lever mechanism for bistable nonlinear energy harvesting under Gaussian-type stochastic excitations. *J Phys D Appl Phys*. 2018;52(5):055501.
16. Yang K, Fei F, An H. Investigation of coupled lever-bistable nonlinear energy harvesters for enhancement of inter-well dynamic response. *Nonlinear Dyn*. 2019;96(4):2369-2392.
17. Yang K, Wang J, Yurchenko D. A double-beam piezo-magneto-elastic wind energy harvester for improving the galloping-based energy harvesting. *Appl Phys Lett*. 2019;115(19):193901.
18. Amini Y, Emdad H, Farid M. Piezoelectric energy harvesting from vertical piezoelectric beams in the horizontal fluid flows. *Sci Iran*. 2017;24(5):2396-2405.
19. Zou Q, Ding L, Wang H, Wang J, Zhang L. Two-degree-of-freedom flow-induced vibration of a rotating circular cylinder. *Ocean Eng*. 2019;191:106505.
20. Jbaily A, Yeung RW. Piezoelectric devices for ocean energy: a brief survey. *J Ocean Eng Marine Energy*. 2014;1(1):101-118.
21. Hobeck JD. Energy harvesting with piezoelectric grass for autonomous self-sustaining sensor networks, in Aerospace Engineering. University of Michigan; 2014.
22. Amini Y, Emdad H, Farid M. An accurate model for numerical prediction of piezoelectric energy harvesting from fluid structure interaction problems. *Smart Mater Struct*. 2014;23(9):095034.
23. Erturk A, Vieira WGR, De Marqui C, Inman DJ. On the energy harvesting potential of piezoaeroelastic systems. *Appl Phys Lett*. 2010;96(18):184103.
24. Akaydın HD, Elvin N, Andreopoulos Y. Experimental study of a self-excited piezoelectric energy harvester. Paper presentend at: ASME 2010 Conference on Smart Materials, Adaptive Structures and Intelligent Systems. Philadelphia, Pennsylvania, USA; 2010. 179-185.
25. Akaydin HD, Elvin N, Andreopoulos Y. The performance of a self-excited fluidic energy harvester. *Smart Mater Struct*. 2012;21(2):025007.
26. Dai H, Abdelkefi A, Wang L. Piezoelectric energy harvesting from concurrent vortex-induced vibrations and base excitations. *Nonlinear Dyn*. 2014;77(3):967-981.
27. Dai H, Abdelkefi A, Wang L. Theoretical modeling and nonlinear analysis of piezoelectric energy harvesting from vortex-induced vibrations. *J Intell Mater Syst Struct*. 2014;25(14):1861-1874.
28. Yang Y, Zhao L, Tang L. Comparative study of tip cross-sections for efficient galloping energy harvesting. *Appl Phys Lett*. 2013;102(6):064105.
29. Zhang M, Wang J. Experimental study on piezoelectric energy harvesting from vortex-induced vibrations and wake-induced vibrations. *J Sens*. 2016;2016:1-7.
30. Wang J, Zhou S, Zhang Z, Yurchenko D. High-performance piezoelectric wind energy harvester with Y-shaped attachments. *Energ Conver Manage*. 2019;181:645-652.
31. Molino-Minero-Re E, Carbonell-Ventura M, Fisac-Fuentes C, Mànuel-Làzaro A, Toma DM. Piezoelectric energy harvesting from induced vortex in water flow. Paper presented at: 2012 IEEE International Instrumentation and Measurement Technology Conference Proceedings; 2012

1099114x, 2020, 5, Downloaded from https://onlinelibrary.wiley.com/doi/10.1002/er.5164 by The Hong Kong University Of Science & Technology, Wiley Online Library on [17/04/2026]. See the Terms and Conditions (https://onlinelibrary.wiley.com/terms-and-conditions) on Wiley Online Library for rules of use; OA articles are governed by the applicable Creative Commons License

32. Mehmood A, Abdelkefi A, Hajj MR, Nayfeh AH, Akhtar I, Nuhait AO. Piezoelectric energy harvesting from vortex-induced vibrations of circular cylinder. *J Sound Vib*. 2013;332(19):4656-4667.
33. Zhang M, Liu YZ, Cao ZM. Modeling of piezoelectric energy harvesting from freely oscillating cylinders in water flow. *Math Probl Eng*. 2014;13.
34. Song R, Shan X, Lv F, Xie T. A study of vortex-induced energy harvesting from water using PZT piezoelectric cantilever with cylindrical extension. *Ceram Int*. 2015;41:S768-S773.
35. Wang J, Hu G, Su Z, et al. A cross-coupled dual-beam for multi-directional energy harvesting from vortex induced vibrations. *Smart Mater Struct*. 2019;28(12):12LT02.
36. Ma Y, Luan Y, Xu W. Hydrodynamic features of three equally spaced, long flexible cylinders undergoing flow-induced vibration. *Eur J Mech B Fluids*. 2020;79:386-400.
37. Unal MF, Rockwell D. On vortex formation from a cylinder. Part 2. Control by splitter-plate interference. *J Fluid Mech*. 1988;190:491-529.
38. Lighthill J. Fundamentals concerning wave loading on offshore structures. *J Fluid Mech*. 1986;173:667-681.
39. Tan W, Wu H, Zhu G. Fluid-structure interaction using lattice Boltzmann method: moving boundary treatment and discussion of compressible effect. *Chem Eng Sci*. 2018;184:273-284.
40. Lallemand P, Luo L-S. Lattice Boltzmann method for moving boundaries. *J Comput Phys*. 2003;184(2):406-421.
41. Sui Y, Chew YT, Roy P, Low HT. A hybrid immersed-boundary and multi-block lattice Boltzmann method for simulating fluid and moving-boundaries interactions. *Int J Numer Methods Fluids*. 2007;53(11):1727-1754.
42. Zhou S, Wang J. Dual serial vortex-induced energy harvesting system for enhanced energy harvesting. *AIP Adv*. 2018;8(7):075221.

How to cite this article: Zhang M, Hu G, Wang J. Bluff body with built-in piezoelectric cantilever for flow-induced energy harvesting. *Int J Energy Res*. 2020;44:3762–3777. https://doi.org/10.1002/er.5164

1099114x, 2020, 5, Downloaded from https://onlinelibrary.wiley.com/doi/10.1002/er.5164 by The Hong Kong University Of Science & Technology, Wiley Online Library on [17/04/2026]. See the Terms and Conditions (https://onlinelibrary.wiley.com/terms-and-conditions) on Wiley Online Library for rules of use; OA articles are governed by the applicable Creative Commons License